Batteries & Supercaps

Review
doi.org/10.1002/batt.202200493

Chemistry Europe
European Chemical Societies Publishing

www.batteries-supercaps.org

VIP *Very Important Paper*

Special Collection

Toward High Energy Density FeF_x ($x = 2$ and 3) Cathodes for Lithium-Ion Batteries

Jun Li,[a, b] Xifei Li,*[a, b] Xiangyang Li,*[c] and Qinting Jiang[a, b]

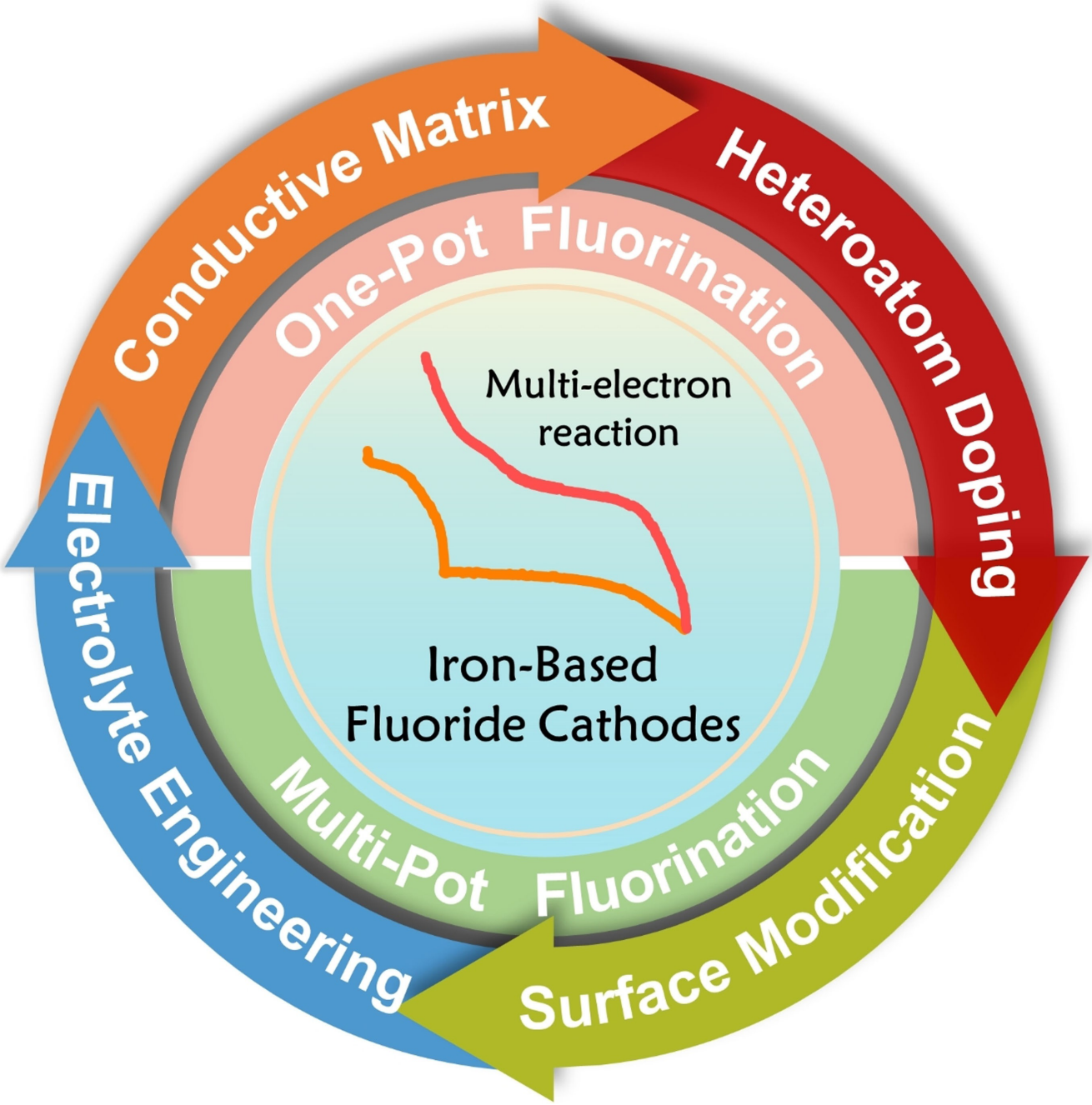

It has been challenging to develop next-generation higher energy density cathode materials to satisfy the incremental demand for lightweight and miniaturization for lithium-ion batteries (LIBs). The iron-based fluoride (FeF_x) cathodes may be highly competitive due to abundant resources as well as high theoretical capacity. However, the complex multiphase conversion reactions of the FeF_x cathodes cause limited battery performance hindering its commercialization. Herein, this review focuses on the multi-electron conversion processes involved in solid-solid reactions. More importantly, the scientific strategies of enhanced FeF_x performance are mainly addressed in view of four critical aspects, i.e., conductive matrix, heteroatom doping, surface modification, and electrolyte engineering. It is demonstrated that the optimized strategies can mitigate the challenges of the FeF_x cathodes during multi-electron conversion processes. It is believed that this review has been a guidance for improving the cycling performance of the FeF_x cathodes for high energy density LIBs.

1. Introduction

Industrial technology development and global carbon neutrality efforts have driven research into green, low-cost and renewable energy.[1–4] Although solar, wind and hydropower have been widely studied in recent years, the application of renewable energy into power systems needs to be improved, and the research to meet the needs of large-scale energy storage systems and green energy is sustaining.[5,6] With the commercialization of lithium-ion batteries (LIBs) and the increase in public acceptance of electric vehicles (EVs), the battery market will reach up to $180 billion in 2030. Owing to the stronger-than-expected growth in the consumer electronics and electric vehicle segments, the cost of module-level LIBs and the volumetric energy density of package-level batteries will be further reduced.[7–9]

With the maturation of battery technology, the commercial layered transition metal oxides cathode materials face limited specific capacity increase. The energy density growth rate of the highest-performance LIBs slowed to only 1–2% per year, making it hard to enhance the energy density of commercial LIBs significantly.[10–14] Meanwhile, the Co-free layered transition metal oxides cathode and Li-rich manganese based on higher capacity are developing rapidly. Whether a major breakthrough can be achieved in the next decade is still controversial.[15–17] Although nickel-rich cathode has great potential to meet the electric vehicles in the future, it may face uncertain price fluctuations and serious environmental problems, which makes it difficult to meet the long-term demand. Consequently, developing low-cost, widely available metals and higher energy density electrodes are considered the most reasonable way to achieve high-specific rechargeable batteries.

As aforementioned, future batteries require breakthroughs in battery chemistry or electrode materials based on redox reactions. The cathode of intercalated compounds lacks reasonable selectivity, and a conversion cathode material "beyond Li-ion" needs to be investigated.[18–20] In a solid-solid reaction, the conversion-type materials increase capacity through multi-electron electrochemical reactions with lithium ions, accompanied by the crystal structure changes and the breaking and reformation of chemical bonds.[21–23]

Among the various candidate conversion cathodes, the metal sulfides and fluorides have been extensively studied for their high electronegativity and theoretical volume capacity.[24,25] Although lithium-sulfur batteries have been used in large unmanned aerial vehicles and portable power supplies, the current relevant reports show that FeF_x has a higher theoretical volume capacity and a more apparent cost advantage in large-scale applications. Specifically, on the one hand, during the lithiation state, FeF_x cathodes have a volumetric energy density (FeF_2: 2002 mAh cm^{-3}, FeF_3: 2196 mAh cm^{-3}) comparable to that of intercalation cathode, and surpassing lithium-sulfur batteries (1935 mAh cm^{-3}).[26,27] On the other hand, the resource of metal iron rich and low costs (illustrated in Figure 1).

The common fluoride sources for synthetic FeF_x include HF, NH_4F, H_2SIF_6, etc., which can usually be obtained from inexpensive fluorine-based minerals or by-products produced in the metallurgical industry to synthesize metal fluoride. In addition, the price of Fe is low, and the economic reserves are 230 Bt, effectively avoiding insufficient production capacity and price fluctuations caused by the rapid growth of Co and Ni demand. Since the LIBs weight is reduced to one-third of the insert-type cathode material, it will be conducive to gaining favor in weight-sensitive fields and becoming a safe, sustainable, and inexpensive LIBs cathodes system. However, the FeF_x cathodes face structural rearrangement and insulating properties during the conversion reactions, resulting in slower kinetic performance and shorter cycle life.[28,29]

Despite these inherent obstacles, in the last decades, a variety of breakthroughs have been achieved in overcoming major scientific problems related to FeF_x cathodes through

[a] J. Li, Prof. X. Li, Q. Jiang
Shaanxi International Joint Research Center of Surface Technology for Energy Storage Materials,
Institute of Advanced Electrochemical Energy and School of Materials Science and Engineering,
Xi'an University of Technology
Xi'an, Shaanxi, 710048 (China)
E-mail: xfli2011@hotmail.com
[b] J. Li, Prof. X. Li, Q. Jiang
China Engineering Research Center of Conducting Materials and Composite Technology, Ministry of Education, Key Laboratory of Advanced Batteries Materials for Electric Vehicles of China Petroleum and Chemical Industry Federation
Xi'an, Shaanxi, 710048 (China)
[c] X. Li
Science and Technology on Electromechanical Dynamic Control Laboratory,
Xi'an Institute of Electromechanical Information Technology
Xi'an 710065 (China)
E-mail: liyang2039@163.com

Special Collection An invited contribution to a Special Collection on IV Symposium on Advanced Energy Storage

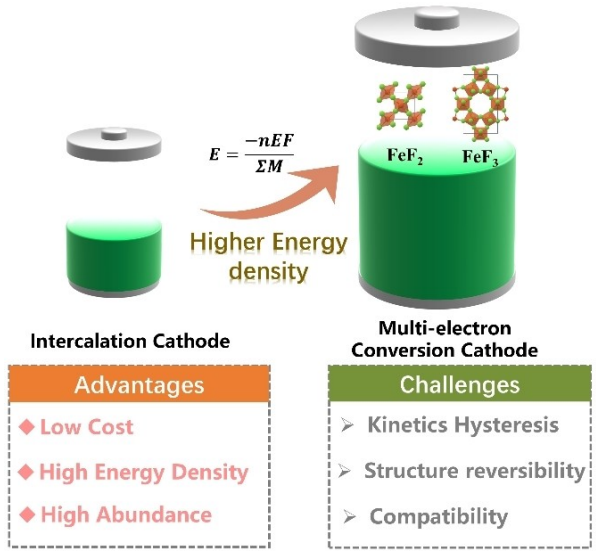

Figure 1. Schematic illustration of energy density of multi-electron reaction versus one electron reaction and advantages and remain challenges.

various FeF_x materials engineering techniques, there is still a large gap with practical industrial applications. To meet the demands of FeF_x cathodes energy storage devices, further in-depth exploration in nanostructure optimization and material design are needed.[30–32]

This review summarizes the latest advances of FeF_x cathodes in LIBs. Firstly, the conversion mechanism and existing challenges of FeF_x cathodes are briefly expounded. Then, the different fluorination synthesis routes of FeF_x are discussed separately. More importantly, the different scientific strategies to enhance the FeF_x conversion kinetics have also been emphasized. Finally, the main practical issues to achieving major breakthroughs were analyzed, and further proposed several potential solutions as guidelines for a shed on the development of FeF_x cathodes.

2. Conversion Chemistry

High capacity is one of the most crucial targets for currently LIBs, and low electron transfer numbers ($n < 1$) limit the energy density of intercalated electrodes.[33] In contrast, exploring multi-electron redox electrodes opens new directions for achieving higher energy density LIBs systems.[34,35] the "multi-electron reaction" is expressed as the number of electrons transferred in a redox reaction. Each transition metal atom accepts multiple electron transfers, delivering 1.5–2 times and 2–3 times volumetric and mass-energy density, respectively. For example, the storage mechanism of FeF_2 is carried out through a three-phase conversion process. During a complex redox reaction, three phases (FeF_2, Fe, LiF) will exist at the same time, Fe nanoparticles are interconnected to form a continuous conductive network to promote local electron conduction.[36,37]

Recently, through further depth study of the reaction mechanism, new insights into the transformation reaction were proposed.[38] Xiao et al. found that the FeF_3 reduction process is mainly controlled by the diffusion step. The fluoride ion sublattice in metal fluoride forms a topological transformation relationship with the generated lithium fluoride in space. At the initial lithiation, FeF_2 is formed on the surface of FeF_3 particles, accompanied by the generation of cationic ordered and disordered $Li_xFe_yF_3$ phase, which are intermediate stages between FeF_2 and LiF, followed by further lithiation directly into LiF and Fe.[39–42] However, the diffusion process generally causes the dissolution and loss of Fe and F in the organic electrolyte and shuttle to the anode interface to form a solid electrolyte interface (SEI) layer. The electrochemical reaction of the electrode interface is disrupted, leading to decreased in cycling stability and Coulombic efficiency.[43]

It needs to be admitted that FeF_x conversion cathode materials still exist multiple limitations before reaching their theoretically attractive features. For example, FeF_x are reduced by Li-ion to form agglomerated Fe nanoparticles (≤ 5 nm) dispersed in an insulating LiF matrix during the lithiation

Jun Li received his master's degree from Lanzhou University of Technology (LUT) in 2020. He is currently a Ph.D. candidate at the Institute of Advanced Electrochemical Energy & School of Materials Science and Engineering under the supervision of Prof. Xifei Li at Xi'an University of Technology. His current research focuses on the material and structure design of iron-based fluoride cathode for high specific energy lithium-ion batteries.

Qinting Jiang received her master's degree from School of Chemistry and Chemical Engineering, Shandong University of Technology (SDUT) in 2020. Now, she is a Ph.D. candidate, under the supervision of Prof. Xifei Li in the Institute of Advanced Electrochemical Energy & School of Materials Science and Engineering, Xi'an University of Technology. Her research focus on the cathodes of lithium-ion batteries, including the structure design, synthesis and mechanism analysis of iron-based fluoride.

Xifei Li is a professor at Xi'an University of Technology. He is an executive editor-in chief of Electrochemical Energy Reviews and a vice-president of International Academy of Electrochemical Energy Science. Dr. Li earned his Bachelor at Harbin Institute of Technology, and he completed his Master and Ph.D. in General Research Institute for Nonferrous Metals of China and Xi'an Jiaotong University, respectively. He then worked as a Postdoctoral Fellow at Florida International University and University of Western Ontario. Dr. Li's research group is working on optimized interfaces of the anodes and the cathodes with various structures for high performance rechargeable batteries.

process. Partially insulated LiF and Fe cannot participate in the reconversion reaction upon delithiation, resulting in limited conversion capacity.[44] Besides, the poor electronic conductivity is mainly caused by the strong ionic character of the Fe–F bond that inevitably affects the electrode kinetic reaction process. Since the true reaction path of the electrode is closely related to the kinetics, the homogeneity reaction (completeness and spatial evolution of each lithiation-delithiation process) is strongly influenced by the reaction kinetics during these consecutive multi-step reactions.[45] As in previous studies, large voltage hysteresis (several hundreds mV to ≈2 V) caused by ohmic voltage drops, uneven active components and reaction overpotentials seriously hindered their practical application.[46,47]

For FeF_x cathodes materials, the crystal structure and the coexistence of separate nanophases always occur during the cycling process. The continuous generation of active sites on the electrode surface leads to the formation of cathode interphase (CEI) layer in a dynamic manner, resulting in a severe and continuous electrolyte consumption.[48] Through the study of different kinds of metal fluorides, the charge transfer impedance of the uncycled electrode is closely related to voltage hysteresis and capacity degradation. During the charging and discharging process, the compound that suffers the largest hysteresis growth and capacity degradation has the largest charge transfer resistance increase, The postmortem analysis found that the formation of undesirable CEI layer is the cause of enlarged resistance.[49] Moreover, the free protons produced by unfavorable electrolyte decomposition cause the dissolution of active material and corrosion of the battery. The rough surface formation on the Li anode also immensely hinders the improvement of FeF_x-based electrodes.[50]

3. Controllable Synthesis

The emergence of FeF_x cathodes provides new opportunities and possibilities for basic research and energy storage development. To solve the aforementioned challenges, many researchers have proposed different synthesis strategies using other fluoride-containing compounds to fabricate nanoscale FeF_x materials to further improve electrochemical properties.[51–53] Among them, the low-temperature solution precipitation chemical process is a classic method for synthesizing FeF_x materials.[54] The method can controllably synthesize of different dimensional channels, which facilitates the rapid Li-ion intercalation in the lattice. Meanwhile, a method of hydrofluoric acid (HF) fluorination that can be handled on a large scale but is extremely dangerous has received much attention. However, neither method can meet the high-yield demand for energy storage devices.[55] To address the aforementioned problems, utilizing different types of fluorine sources in the fluorination synthesis routes, including HF, ammonium fluoride (NH_4F), ionic liquids (ILs), hexafluorosilicic acid (H_2SiF_6) and fluorine-containing gas (such as NF_3), has been widely developed in the energy storage fields.[56–60] Hence, in this review, the current synthesis methods are grouped according to their fluorination processes (one-pot fluorination and multi-pot fluorination), and their advantages and disadvantages are discussed.

3.1. One-pot fluorination

In comparison to multi-pot fluorination methods for synthesizing FeF_x materials, one-pot fluorination greatly reduces time and cost, which is more attractive for practical applications. It has been a rapidly evolving field of research since it is reported. Li et al.[61] excelled in this field, for the first time, using 1-butyl-3-methylimidazolium tetrafluoroborate ILs ($BmimBF_4$) as the F-sources to achieve a simple synthesis route. After adding $Fe(NO_3)_3 \cdot 9H_2O$ into $BmimBF_4$ solution, the solvated Fe^{3+} combined with F^- to form iron-based fluoride precursor precipitation, and further low-temperature drying treatment directly generated hexagonal tungsten bronze (HTB) phase $FeF_3 \cdot 0.33H_2O$ (Figure 2a). HTB type $FeF_3 \cdot 0.33H_2O$ has two Fe–F octahedrons linked by corner-sharing of coordinated fluorine atoms, forming one-dimensional hexagonal tunnels along the [001] direction. The unique open tunnel structure facilitates Li^+ transport and storage, and its porous structure is conducive to the infiltration of the electrolyte, while the H_2O molecules in the tunnel play a role in stabilizing the open framework skeleton. Except as an essential fluoride source, the $BmimBF_4$ ILs also act as nanostructure-controlled solvents and soft templates. What's more, using ILs as fluorine sources, the pyrochlore structural iron-based fluoride is developed via a solvothermal self-assembly process.[62,63] By controlling the synthesis temperature, reaction time and the amount of ILs, a series of hydrated pyrochlore iron-based fluoride materials with different morphologies and phases are synthesized. The pyrochlore phase has internally connected three-dimensional ion channels. Compared with HTB-type fluoride, the cavities connect by sharing hexagonal faces, forming internally connected ion channels. The H_2O molecules are restrained in the tetrahedral cavity, which may be more beneficial to the insertion of Li^+. The introduction of ILs in these led to the hydrolysis of weakly coordinated BF_4^- under heating conditions to give BF_3^- and F^-, followed by the reaction of solvated Fe^{3+} with F^- to form a series of iron-based fluoride nanoparticle precipitates.

The non-aqueous chemical synthesis has multiple advantages. Firstly, the overall reaction process is close to room temperature without further high-temperature calcination. Secondly, compared with other corrosive fluoride sources (such as HF), ILs have environmentally friendly and safety characteristics to operate as fluoride sources. Besides, ILs effectively limit particle agglomeration to form uniform nanocrystals.[64] In subsequent work, they also found that ILs-cations as structural guide agents significantly affected the nucleation/growth process of pyrochlorite phase.[54] Different sizes of ILs-cations evidently affect the surface defect concentration and cavity size of FeF_x materials, providing a reference for exploring open structural prototypes of fluorinated frameworks. Whereas the high cost and elaborate synthesis process may still have doubts about future continuous research. In addition to ILs,

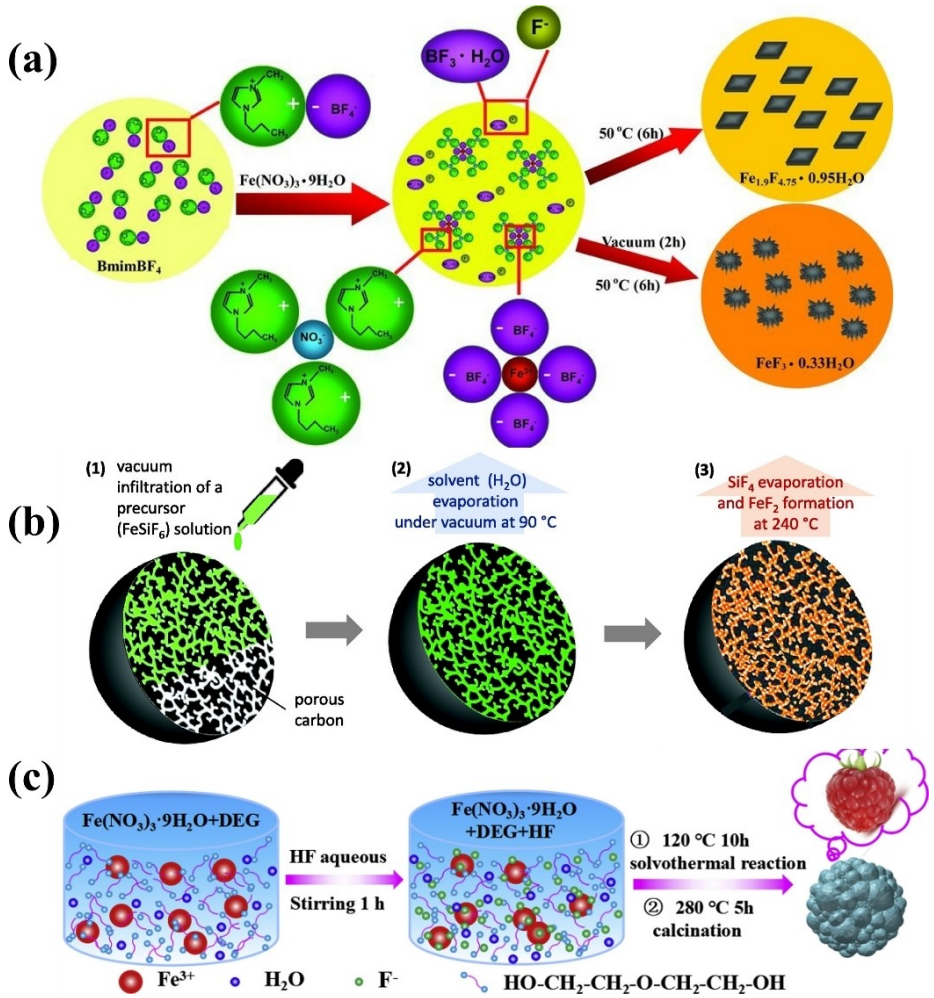

Figure 2. One-pot fluorination methods: a) Scheme of FeF_x formation mechanism from ionic liquids fluorine source. Reproduced with permission from Ref. [61]. Copyright (2010) Wiley-VCH. b) Scheme of FeF_x formation mechanism from H_2SiF_4 fluorine source. Reproduced with permission from Ref. [66]. Copyright (2015) Wiley-VCH. c) Scheme of FeF_x formation mechanism from HF fluorine source. Reproduced with permission from Ref. [43]. Copyright (2020) Elsevier B.V.

$FeF_3 \cdot 0.33H_2O$ powder can also be synthesized by NH_4F as a fluorine source through the liquid phase method.[65] $Fe(NO_3)_3 \cdot 9H_2O$ and NH_4F are used as iron and fluorine sources, and polyethylene glycol is utilized as a dispersant. A white $FeF_3 \cdot 3H_2O$ precursor precipitate is produced by adding NH_4F aqueous solution drop by drop to an iron-containing solution. The crystal water was further removed by calcination precursor under an argon atmosphere. Finally, the $FeF_3 \cdot 0.33H_2O$ powder is obtained.

To address above-mentioned limitations, a vacuum-infiltrating setup to infiltrate the nearly-saturated $FeSiF_6$ precursor drop by drop into a porous carbon matrix was developed.[66] The capillary force was utilized in the drying process to ensure the $FeSiF_6$ nanoparticles precipitation inside the carbon pores and further thermally decomposed into FeF_2 nanoparticles at a low temperature of 240 °C (Figure 2b). On the basis of the previous procedure, Gorden et al.[49] synthesized metal difluoride (m-MF_2) and multi-walled carbon nanotube (MWCNT) nanocomposites via solid-solution mixed. By adjusting the molar ratio of the two elements, the different kinds of mixed m-MF_2-MWCNT nanocomposites were achieved. In addition, the $FeF_3 \cdot 3H_2O$ composites can be obtained by utilizing the low-temperature liquid phase reaction method, which directly adds the HF into the iron hydroxide precursor solution by continuous stirring in the Teflon bottle.[67] Subsequently, through a one-step solvothermal method to synthesize different various morphology FeF_x samples by controlling the HF concentration and reaction time.[43] The pure $FeF_3 \cdot 0.33H_2O$ with high crystallinity has a positive correlation with water in the reaction system, indicating that HF solution not only serves as F source but also precisely regulates the morphology and phase of the FeF_x materials (Figure 2c).

The conversion iron oxyfluoride material is a promising cathode candidate, where the covalent Fe–O bonding of the highly ionic fluoride enhances the electronic conductivity. The current solid-state based synthesis methods have many limitations. Recently, a mild wet chemical strategy with alcoholysis-assisted hydrolysis reactions has been successfully developed.[68,69] Using $FeF_3 \cdot 3H_2O$ and ethanol as reactants and solvents, the composition/structure of the obtained FeOF can

be significantly controlled by controlling the molecular structure of the alcohols. Introducing appropriate vacancy defects is a vital strategy to improve the metal fluoride-lithium storage performance. In recent studies, a microwave-assisted hydrothermal synthesis method of iron-based oxy-hydroxy fluorides has been successfully proposed. The thermal behavior has shown that the thermal treatment temperature is critical for the generation of iron-based oxy-hydroxy fluorides with different anions.[70,71] Between room temperature and 350 °C, the dehydroxylation continued without any fluorine loss. In the range of 200–350 °C, different chemical components can be adjusted depending on the content of OH^-/O^{2-} and structural water. In addition, the atomic pair distribution function (PDF) and Mössbauer studies show that the formation of amorphous iron oxides can be effectively avoided when the annealing temperature is 300 °C to 350 °C.

Ammonium hexafluoroferrate $[(NH_4)_3FeF_6]$ is another solid precursor for synthesizing of FeF_x materials with slight environmental impact. Based on this, the FeF_3 composites with various microstructures were synthesized by the precursor-mediated method.[72] The precursor of $(NH_4)_3FeF_6$ was thermally decomposed into FeF_3, and its morphology and crystallinity could be adjusted by changing the ethanol/water volume ratio during precipitation. Xiao et al.[38] similarly synthesize a single-crystalline, monodisperse FeF_2 nanorods by using Iron(II) trifluoroacetate as a single F and Fe precursor. However, the precisely controlled synthesis process needs to be further optimized.

3.2. Multi-pot fluorination

Currently, multi-pot fluorination is the most common method to prepare FeF_x materials, mainly formed by fluorination of the external fluoride source during the synthesis of iron-based precursor. A novel vapor-solid method was reported for synthesizing of FeF_3 composites in a Teflon cylinder.[73] The process involves transferring the iron-based precursor to a smaller Teflon cylinder, then placing the entire Teflon cylinder in a large capacity Teflon autoclave preloaded with an amount of HF. With the evaporation of HF solution at low temperature, the iron precursor gradually transformed into FeF_x complex. Recently, Li et al.[74] used an analogous approach to fluorine Fe_3O_4 precursor to FeF_3 nanomaterials (Figure 3a). It is worth noting that the phase change leads to an increase in the diameter of the nanosphere and sample has almost the same spherical morphology as the Fe_2O_3 precursor, maintaining the same mass ratio of Fe, while F atoms replace all O atoms.

Based on the concept of scalable and low-cost development, a simple and universal solid-solid fluorination synthesis method was developed with NH_4F as the fluorine source.

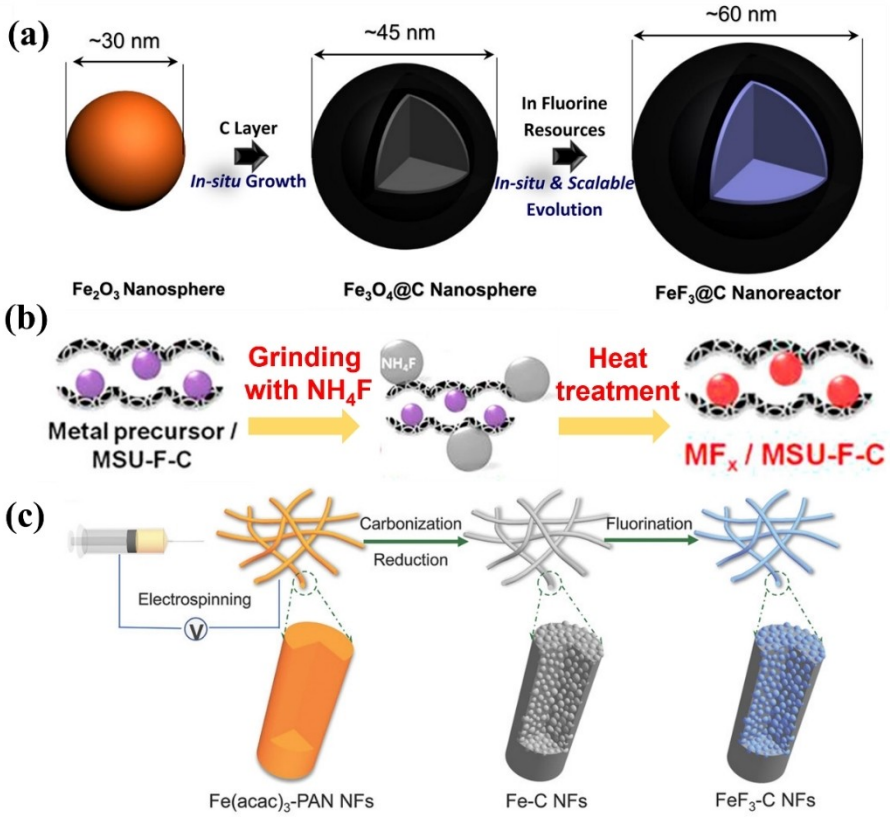

Figure 3. Multi-pot fluorination methods: a) Scheme of FeF_3@C formation mechanism from HF fluorine source. Reproduced with permission from Ref. [74]. Copyright (2017) American Chemical Society. b) Scheme of FeF_x formation mechanism from NH_4F fluorine source. Reproduced with permission from Ref. [75]. Copyright (2016) American Chemical Society. c) Scheme of FeF_3–C nanofibers formation mechanism from NF_3 fluorine source. Reproduced with permission from Ref. [79]. Copyright (2018) Wiley-VCH.

(Figure 3b) Excessive NH_4F is mechanically ground with the iron-based precursor, and heat treatment is carried out in a tubular furnace under an inert atmosphere, which converts metal precursor into anhydrous FeF_x materials. The unique synthesis method has several advantages over previously reported. (1) Although small amounts of F-containing by-products are inevitably produced, the whole process is a simple operation and relatively safe, avoiding using highly toxic compounds (such as F_2 or HF) as fluorine sources. (2) Moisture sensitive and easily defluorinated CuF_2 can be directly synthesized. (3) The reaction avoids the decrease in yield caused by the partial dissolution of liquid-phase fluorination.[75,76]

Recently, a more flexible gas-phase fluoride method for designing and synthesis of nanostructured metal fluoride has developed rapidly.[65,77,78] Yushin's group has done a lot of work on this, developing a range of FeF_3 cathode materials based on electrostatic spinning technology. A directly fluorinated Fe–C nanofibers composites under the flow of low concentration NF_3 gas to obtain FeF_3–CNT nanomaterials.[79] The fluorinated FeF_3–CNT composites maintain the initial morphology of nanofibers except for the increased size of FeF_3 particles (Figure 3c). Different from the aforementioned fluorination reaction using highly corrosive fluorine sources, gas fluorination ensures the integrity and uniformity of the primary morphology to the greatest extent. Furthermore, NF_3 is commonly used in the dry etching process in semiconductor manufacturing, widely available chemical. When using low concentrations of NF_3 gas, the solid-gas phase reaction is simple and speedy. As a general gas-phase fluorination method, it can be widely extended to the synthesis of other metal fluorides and has great potential in the future.[80] Overall, the fluorination processes based on the different fluoride sources have been used to synthesis of Fe-based fluorides.

The tetragonal tungsten bronze (TTB) phase $K_{0.6}FeF_3$ can be obtained by grinding and mixing KF, FeF_2 and pre-prepared $FeF_3 \cdot 0.33H_2O$ and annealing at 300 °C for a certain time in an inert atmosphere.[81] The TTB phase can be obtained by topological densification of the HTB phase, where the Fe–F octahedral connect is altered. Resulting in the hexagonal side tunnel in HTB being transformed into pentagonal and tetragonal cavities.[82,83] The TTB phase replaces the H_2O molecules with potassium ions with better thermal stability as channel filler. In addition, different types of metal fluorides can be synthesized using changes in the metal source. Various forms of metal phases (or metal compounds) are efficiently converted into metal fluorides by one or multi-step fluorination reactions using fluorine-containing compounds, examples include NiF_2, CoF_2, CoF_3, and CuF_2, etc. In recent work, CoF_2/C nanocomposites were successfully prepared using direct low-temperature gas fluorination of metal-organic-framework-derived Co/C nanocomposites, with the samples simultaneously maintaining their original morphology/structure.[29] Highly valued metal fluorides such as CoF_3 usually decompose into CoF_2. Despite these limitations, Groult et al. obtained nano-CoF_3 particles directly using F_2 gas by optimizing the synthesis conditions. The elaborate fluorination process allows for the direct fluorination of Co particles into nano-CoF_3 particles, accompanied by an increase in nanoparticle size as the fluorination temperature increases.[84,85] Moreover, NiF_2/porous carbon composites were obtained by direct mixing of NH_4F with nickel precursors/porous carbon composites and heating at a certain of temperature under an inert atmosphere.[86] It was demonstrated that the above fluorination approach has good universality.

As the most widely used fluorine source, HF application processes must strictly consider safety and environmental issues due to the hazardous factor. IL-based fluorine sources are much less toxic and more environmentally friendly than HF, but the synthesis process of ILs is complex and expensive. In addition, despite the wide range of solid fluoride sources, the fluorination process is uncontrollable, and it is difficult to construct nano-sized metal fluorides accurately. The gas phase fluorination method is more flexible in morphology design and fluorination degree control. However, the strict requirements for fluorination equipment and related technologies are only verified at the experimental level, which restricts the large-scale application of gas-phase fluorination technology. Therefore, in synthesizing FeF_x materials, the fluorination technology should be comprehensively considered according to the material characteristics and experimental process.

4. Strategies of Improved FeF_x Performance

4.1. Conductive matrix

Various recent studies have reported the application of conductive matrix materials in FeF_x cathodes. Wherein, carbon-based FeF_x composites have been the preferred method to optimize the electrochemical properties of FeF_x cathodes.[87,88] Carbon materials have tunable structures and excellent mechanical stability, providing sufficient active sites and promoting interfacial ion diffusion. It plays a crucial role in the electron/ion transport and structural stability of FeF_x cathodes. A series of carbon-based materials, including graphene, porous carbon and MXene, etc. are widely used as matrix materials for FeF_x cathodes. With the development of different types and sizes of carbon materials, it shows great potential in FeF_x cathodes.

Developing in-situ generation of conductive carbon matrix around FeF_x nanoparticles is an effective way to overcome the problems of low electronic conductivity, volume change and Fe dissolution.[89] A hierarchical carbon wrapped $FeF_3 \cdot 0.33H_2O$@C nanocomposites with pomegranate structure by hydrothermal and solid-state methods was fabricated (Figure 4a).[90] The heterogeneous carbon structure with pomegranate structure effectively reduces the electrochemical polarization, creating an elastic buffer space to alleviate the volume expansion during the lithiation. As a result, the as-prepared $FeF_3 \cdot 0.33H_2O$@C cathode exhibited a discharge capacity of 225 $mAh\,g^{-1}$ at 0.1C (1C = 237 $mA\,g^{-1}$) and a capacity retention of 93% over 200 cycles. Recently, a porous heterostructure of FeF_3 nanocrystal clusters (3–9 nm) wrapped by carbon nanocages was reported (Figure 4b).[91] By confining small FeF_3 nanocrystals

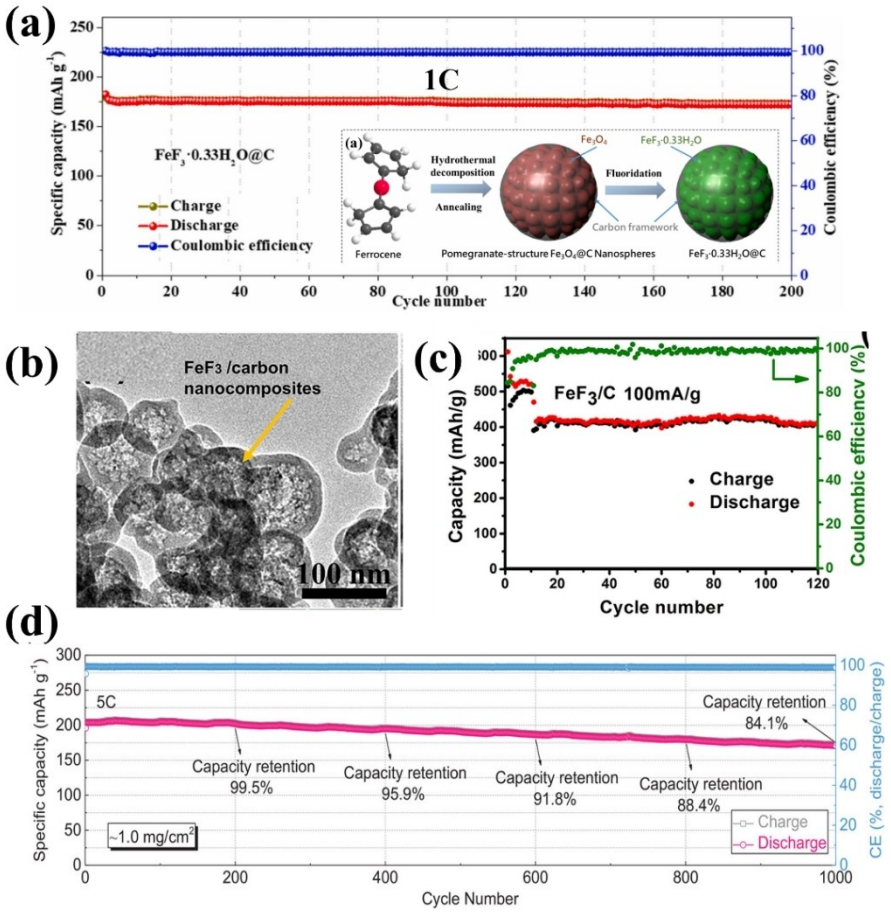

Figure 4. Strategy of conductive matrix designs: a) Hierarchical pomegranate structure carbon wrapped $FeF_3 \cdot 0.33H_2O$. Reproduced with permission from Ref. [90]. Copyright (2022) Elsevier B.V. b and c) FeF_3 nanocrystals (3–9 nm) capsulated in conductive carbon nanocages. Reproduced with permission from Ref. [91]. Copyright (2022) Elsevier B.V. d) 3D honeycomb FeF_3@C composite. Reproduced with permission from Ref. [92]. Copyright (2019) Wiley-VCH.

within the matrix to form a conductive network, which effectively shortens the Li-ion transfer distance and provides abundant electrochemical conversion reaction active sites. Ideally, the interconnected carbon nanocages confine complex transformation reactions to a limited space and enhance the reversibility of the electrodes. As a result, the composites displayed an ultra-high discharge reversible capacity of 410 mAh g^{-1} at 0.1 A g^{-1} in the voltage range of 1.0–4.0 V (Figure 4c).

The three-dimensional (3D) porous structure has additional Li-ion storage sites and ion diffusion channels to evidently boosts the electrode transfer kinetics. Meanwhile, the 3D hexagonal channels can alleviate the volume changes with repeated ions insertion/extraction. Lately, a 3D honeycomb structures FeF_3@C composites were prepared by the sol-gel method.[92] The isolated FeF_3 nanoparticles (10–50 nm) are uniformly embedded in the 3D nanosheets skeleton, and the interconnected honeycomb nanosheets achieve fast electron transfer and ion diffusion simultaneously. Moreover, the FeF_3@C cathode with an areal loading of 5.3 mg cm^{-2}, exhibited a small voltage hysteresis in conventional carbonate-based electrolytes. At a mass loading of 1 mg cm^{-2}, the FeF_3@C electrode offers a high capacity retention of 84.1 % over 1000 cycles (Figure 4d). This work shows that FeF_x cathodes provide higher energy densities than current commercial LIBs even through single-electron reactions. It has landmark significance for the design of other conversion materials based on 3D porous structures.

Graphene (GO) is a popular material in the design of nanocomposite electrode materials due to its unique 2D sheet structure and excellent electrical conductivity. For instance, $FeF_3 \cdot 0.33H_2O$/rGO nanocomposites were fabricated using rGO powders and commercial $FeF_3 \cdot 3H_2O$ as raw material by top-down method and electrostatic self-assembly process.[93] The nanoscale $FeF_3 \cdot 0.33H_2O$ particles are anchored on rGO sheets to ensure close contact between the conductive matrix and the active particles. As a result, the as-prepared $FeF_3 \cdot 0.33H_2O$/rGO delivered a reversible discharge capacity of 175 mAh g^{-1} at 0.5 C over 100 cycles. Very recently, during the synthesis process of free-standing FeF_3/C/rGO film (Figure 5a), the chemical cross-linking properties of chitosan lead to the self-assembly of Fe_2O_3 and rGO into hydrogels with a 3D framework. After the freeze-drying and subsequent compression, a compact Fe_2O_3/C/RGO film was obtained. The as-prepared film was fluorinated and transformed into FeF_3/C/RGO film, which exhibited a metallic luster and high flexibility.[94] The prepared films avoid using PVDF binder and carbon black further to

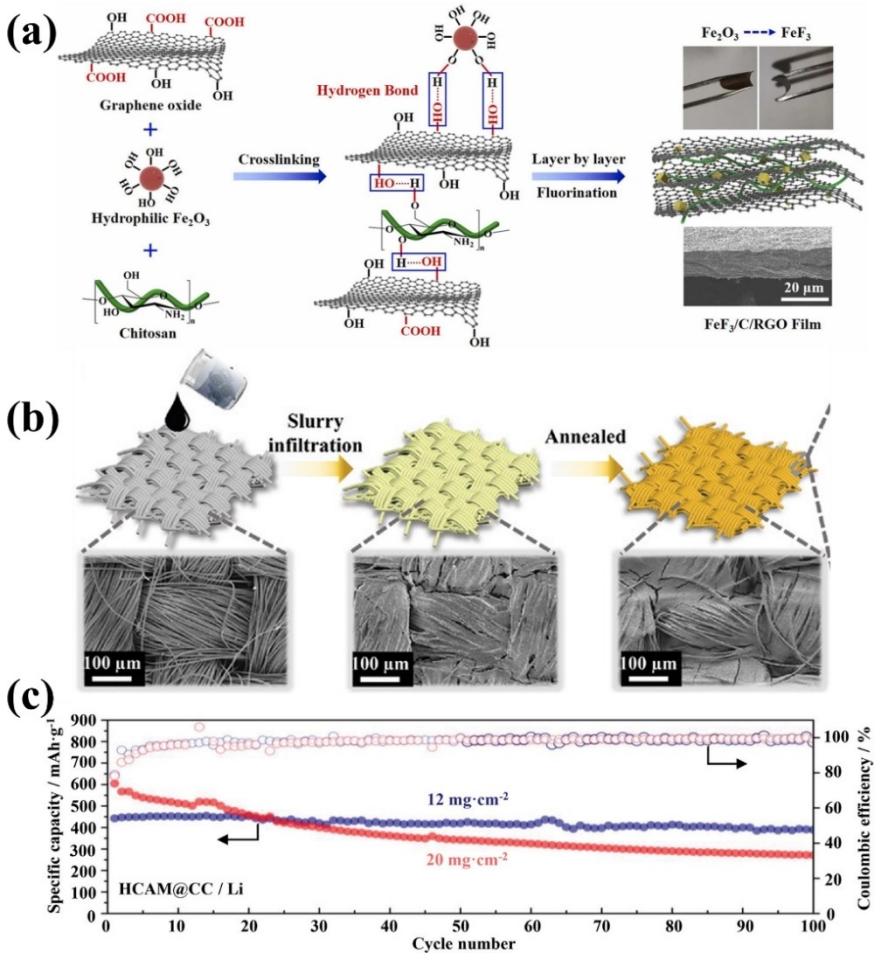

Figure 5. Strategy of conductive matrix designs: a) Synthetic procedure of free-standing FeF_3/C/RGO film. Reproduced with permission from Ref. [94]. Copyright (2022) Elsevier B.V. b) and c) Slurry infiltration method to fabricate FeF_2/CC electrode. Reproduced with permission from Ref. [98]. Copyright (2022) Wiley-VCH.

increase the energy density at high mass loading. Benefiting from the "physical constraints" of the free-standing structure, the FeF_3/C/rGO film electrode attained a high capacity of 220 mAh g^{-1} over 200 cycles at 0.1 A g^{-1}.

Carbon nanotubes (CNTs) and nanofibers (CNFs) have similar physicochemical properties and 1D morphological characteristics.[95,96] The conductive 1D carbon network not only distinctly restricts the FeF_x nanoparticles within a conductive matrix but also minimizes adverse reactions with liquid electrolytes. Thanks to this, a 3D conductive network structure $FeF_3 \cdot 0.33H_2O$/CNTs/GO composite was fabricated using 1D CNTs and 2D porous GO as a conductive carbon matrix.[97] The $FeF_3 \cdot 0.33H_2O$ particles are embedded in the carbon matrix surface and graphene layer, enormously increasing the mass loading and volumetric energy density. Under a mass loading of 5 mg cm^{-2}, a reversible capacity of 148 mAh g^{-1} at 0.84 C was achieved. Recently, a slurry infiltration method to fabricate electrodes with tunable mass loading by permeating a slurry containing FeF_2 nanoparticles into a porous carbon cloth (CC) substrate was proposed (Figure 5b).[98] The FeF_2 nanoparticles, CNTs and CC are intertwined to form a hierarchical electron conduction network. The structure design avoids electrode cracking and delamination under high mass loading conditions, ensuring that the electrodes are capable of fast Li^+ kinetic processes. As a consequence, the FeF_2/CC cathode displayed a discharge capacity of 300 mAh g^{-1} at 1C and an ultra-long cycle life of 4500 cycles. Meanwhile, a record high area capacity of over 6 mAh cm^{-2} is achieved with a mass loading of 20 mg cm^{-2} (Figure 5c).

4.2. Heteroatom doping

Apart from the conductive matrix design, heteroatom doping is an available strategy for altering and regulating the electronic structure by binding specific cations/anions in the host crystal lattice. Heteroatom doping plays a key role in the atomic-scale structure, electronic distribution, surface energy and chemical activity. For FeF_x cathodes, a proper amount of doping can produce sufficient structural defects to facilitate the Li-ion diffusion into the bulk phase. At the same time, doping ions are used as reaction sites to further enhance the Li-ion storage capability.[99]

To further improve the electrochemical reaction kinetics, the low-valent cations can be used to replace high-valent cations to generate charge compensation cavities, which optimizes the electronic structure to enhance the electrode conductivity. For instance, the Ni-doped $FeF_3 \cdot 0.33H_2O$ cathode was prepared by a solvothermal method.[56] The doped of heterovalent cation Ni^{2+} reduces the band gap and intrinsic conductivity of the $FeF_3 \cdot 0.33H_2O$ cathode by producing fluorine vacancies. However, the amount of ion doping is not positively correlated with electrochemical properties but is related to the antagonistic effect of crystal growth. Similar ideas to enhance rate capability by cations doping strategy were also studied, including Ti, Mn and Cr directly doping in FeF_x cathodes.[100–102]

It is particularly important to explore the appropriate doping amount for structural optimization. Very recently, Liu et al.[103] prepared a 3D rod-like Nb doping $FeF_3 \cdot 0.33H_2O$ nanocrystals. Experimental and density functional theory calculations confirm the partial substitution of Nb^{5+} as Fe^{3+} into the $FeF_3 \cdot 0.33H_2O$ crystal phase (Figure 6a). The intrinsic electronic conductivity of the composite is improved by narrowing the band gap, thereby accelerating the electrochemical activity. The as prepared Nb-doped $FeF_3 \cdot 0.33H_2O$@C delivered a high-rate capacity of 187.8 mAh g^{-1} at a high current density of 5C (Figure 6b).

Furthermore, the study confirmed that O substitution also shows an enhanced cyclic performance, high average lithiation/delithiation potential and improved specific capacity. Meanwhile, FeOF offers a higher theoretical capacity of 885 mAh g^{-1} than FeF_2 and FeF_3 in the fully converted state, demonstrating great potential for further exploration.

Considering the previous efforts to doping anions or cations in FeF_x cathodes, the co-doping strategy could be implemented by combining different heteroatoms.[105,106] For example, Fan et al.[107] developed the $Fe_{0.9}Co_{0.1}OF$ cathode by Co and O co-substitution strategy, which achieved a rate capability of 340 mAh g^{-1} at 0.64 A g^{-1} by suppressed less-reversible conversion reaction and reducing the voltage hysteresis (Figure 6c and d). Further analysis of the structure evolution by In-situ synchronous X-ray technology and in-situ transmission electron microscopy showed that the diffusion channel of Li^+ was changed from 3D to 2D and the local structure-oriented rearrangement from corner-sharing octahedra to edge-sharing octahedrons (Figure 6e).[108]

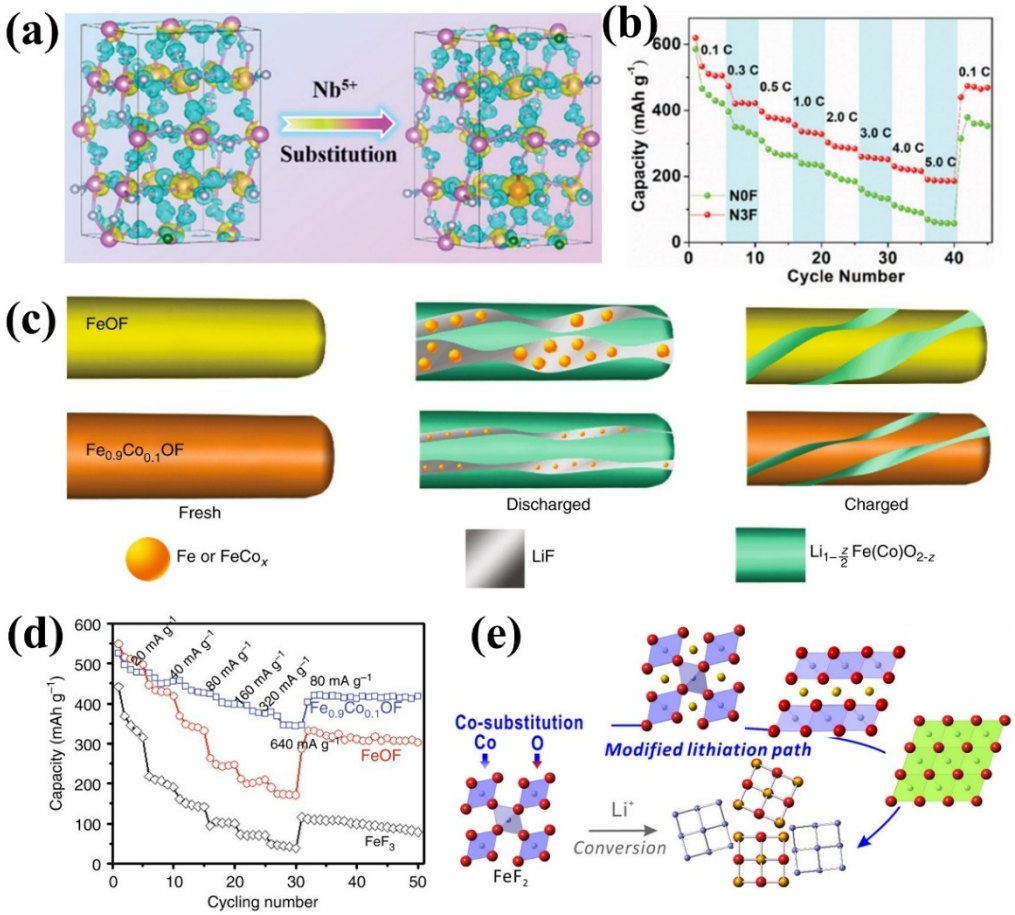

Figure 6. Strategy of heteroatom doping designs: a) Nb-doping $FeF_3 \cdot 0.33H_2O$@C mechanism. b) rate capacity of Nb doping $FeF_3 \cdot 0.33H_2O$@C. Reproduced with permission from Ref. [103]. Copyright (2021) Wiley-VCH. c) Structural evolution for FeOF and $Fe_{0.9}Co_{0.1}OF$ during lithiation. d) Rate capability for $Fe_{0.9}Co_{0.1}OF$ electrode. Reproduced with permission from Ref. [107]. Copyright (2018) Springer Nature. e) Atomic structural changes with inserting Li into FeCoOF. Reproduced with permission from Ref. [108]. Copyright (2020) American Chemical Society.

4.3. Surface modification

The CEI layer growth is usually related to the parasitic chemical reactions of electrolytes on the electrode surface, and the unstable CEI layer continuously consumes the electrolyte and shortens the battery lifetime. Various novel methods have been attempted to stabilize the electrode-electrolyte interface, such as adding functional additives to the electrolyte or special surface treatments of the electrode. For example, a PVDF-based artificial CEI layer coated on FeF_2 nanocrystals (FeF_2@G-P) was prepared by a one-step solvent-thermal method.[109] Owing to the thermal stability and sufficient strength of PVDF, the FeF_2@G-P electrode effectively prevents the Fe dissolution and cracking of FeF_2 particles (Figure 7a). As a result, the FeF_2@G-P composite displayed a discharge capacity of 313 mAh g^{-1} at 0.1 A g^{-1} over 150 cycles.

In recent study, a Ni-supported 3D Al_2O_3-coated FeF_2 electrode was developed.[110] Such an artificial modification layer is produced by a high preciseness and flexibility inorganic cover layer through atomic layer deposition (ALD) technology. The ALD technique produces uniform films in a self-limiting chemisorption vapor precursor, and the resultant coatings are typically a few nanometers or sub nanometers thick. By careful design and synthesis of an ALD layer on the FeF_x electrodes surface, the FeF_x cathodes conversion reactions can be controlled to a certain extent.[111,112] The study manifests that the Al_2O_3 coating reduces the direct contact between the electrode and the electrolyte, enhancing capacity retention without inhibiting electrode reaction kinetics. Subsequently, A similar chemical coating method was performed in FeF_3 cathode, Zhao et al.[113] proposed a double surface protection layer to constructable to deliver a superior capacity retention of over 90% after 300 cycles.

Further, a lithium phosphorus oxynitride (LIPON) protective coating was proposed as an artificial SEI layer on composite electrodes.[114] The mechanistic investigation results show that the thin LIPON layer plays a pivotal role in modulating the electrochemical reaction during the full discharge state, allowing Li-ion permeation but suppressing an excessive conversion reaction. The entire reaction prevents materials crushing and insulating lithium compounds caused by the conversion process and effectively improves the cycling stability.

Apart from optimizing structural stability through ALD, an appropriate amount of multifunctional coating is also a promising option as a protective layer. Lately, FeF_2 nanorod

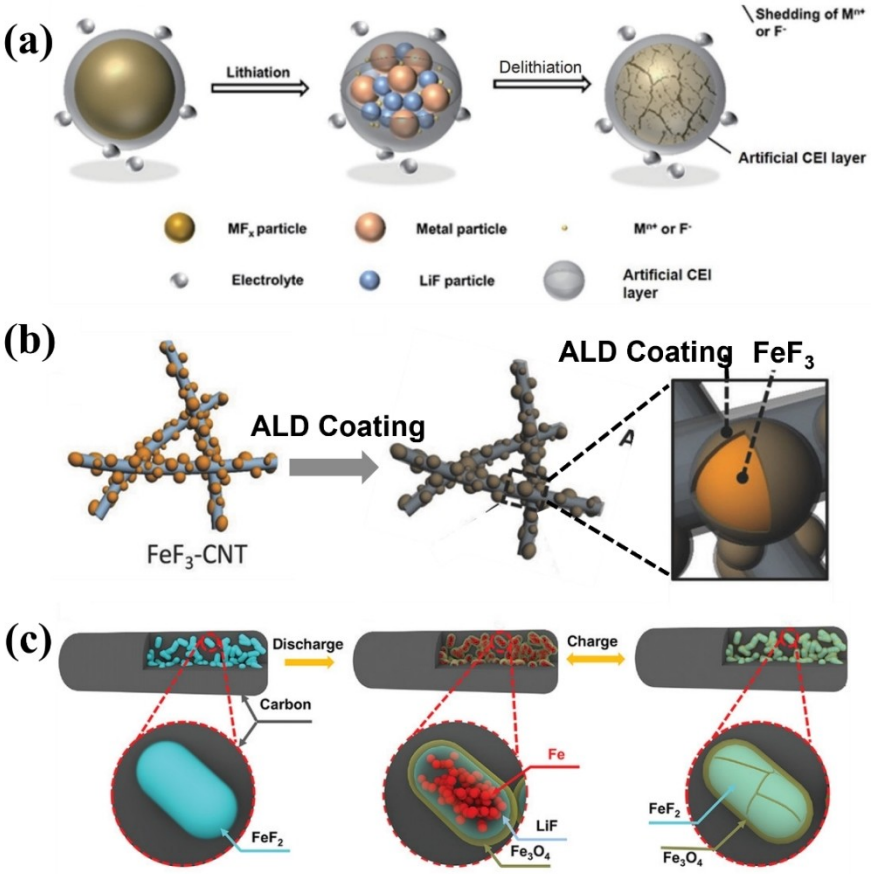

Figure 7. Strategy of surface modification designs: a) illustrated on a PVDF-based artificial CEI layer coated on FeF_2 nanocrystals. Reproduced with permission from Ref. [109]. Copyright (2021) Springer Nature. b) Schematic illustration of the synthesis of ALD coating FeF_3 nanofiber. Reproduced with permission from Ref. [113]. Copyright (2018) Wiley-VCH. c) Schematic of the FeF_2@PDC composite during the initial charge/discharge. Reproduced with permission from Ref. [31]. Copyright (2022) Wiley-VCH.

embedded in a polymer-derived carbon (FeF_2@PDC) matrix composite was reported (Figure 7c).[31] The solid Fe_3O_4 layer is formed in-situ on the FeF_2 composite surface during the first discharge, preventing adverse electrode/electrolyte interface reactions and dissolution of the active components after long cycles. Consequently, the FeF_2@PDC electrode exhibited excellent electrochemical performance, including a record long cycle lifetime of 1900 cycles at 0.5C over 500 mAh g^{-1} and a reversible capacity of 107 mAh g^{-1} at a record rate of 60C. Moreover, an ultra-thin Li_3FeF_6 layer (1 nm) was coated in-situ on the surface of FeF_3 $0.33H_2O$ particles, which also reduced the dissolution and side reactions of the interface during the cycling.[115] These results suggest that the in-situ coating layer effectively enhances the electrochemical performance of FeF_x cathodes.

For the purpose of eliminating the inferior cycle life caused by massive volume expansion. A FeF_3@carbon hybrid was reported via a rapid chemical vapor deposition process. The outer carbon buffer shell effectively offsets the shortcomings mainly caused by structural reconfigurations of the FeF_3 cathode.[74] the cycling stability can be significantly improved by overcoming the weak bonding between the FeF_x materials and the conductive matrix. Furthermore, MoO_3,[116] TiO_2[117] and amorphous carbon,[118] etc. have also been successfully developed as surface modification layers. Additionally, using the conductive polymer PEDOT as a coating layer on FeF_x surface distinctly reduces the capacity decay and maintains a high discharge energy density, both of which possess tightly connected structures with enormous active sites and remarkable electrical conduction, thus enabling significantly enhanced electrochemical kinetics in the conversion process to deliver high reversible capacities.[119]

4.4. Electrolyte engineering

The electrolyte directly determines the ion transport characteristics of the electrolyte-electrode interface and further directly affects the battery performance. The compatibility between the chemical composition of different electrolytes and the cathode material significantly impacts the electrochemical behavior.[120] The most common electrolyte composing $LiPF_6$ solution in cyclic and chain carbonate, which have low viscosity and good ionic conductivity. However, once conversion reactions are involved, the FeF_x electrochemical reversibility in traditional electrolytes is still a great challenge.

The current common cathode electrolyte modification strategies fail to address the conversion kinetics of FeF_x cathodes. Especially in the lithiation process, the existence of uneven precipitation insulating LiF on the whole electrode surface leads to a large voltage hysteresis and rapid capacity decay. Recently, researchers have developed a variety of electrolytes based on material design, significantly improving the reaction environment and optimizing the electrochemical performance.

It is essential to investigate the effect of solvent structure on the cycling performance of FeF_x electrodes. Recent studies have shown that in chain carbonate electrolytes (such as DMC), the electrode surface is completely covered by an interlayer formed by the decomposition of the CEI layer.[121] The increasing interlayer thickness prevents the subsequent conversion reaction and leads to the rapid degradation of the FeF_3 cathode. In contrast, the uniform CEI layer produced by carbonate electrolytes such as EC and PC in the FeF_3 electrode shows good cycling behavior.

In addition to carbonate electrolytes, ether-based electrolytes have also been explored in FeF_x LIBs. A high concentration of 4.6 M lithium difluorosulfonimide (LiFSI) salts in dimethoxyethane (DME) electrolyte was introduced into FeF_x cathodes.[58] The Li-ion permeability protective layer induced by 4.6 M LiFSI in DME electrolyte evidently reduces the capacity loss during the cycling. As a consequence, the electrodes exhibited excellent capacity retention of 63% over 1000 cycles. Huang et al.[122] systematically studied the effects of solvent composition, Li salt composition, concentration and cycling voltage range on FeF_x cathodes performance. The results show that DME-based electrolytes have better rate performance than carbonate electrolytes. Therefore, the LiFSI in DME electrolyte has favorable electrochemical properties and minimal voltage hysteresis in DME-based electrolytes, exhibiting excellent capacity retention of 80% over 100 cycles.

Due to the inherent solid-solid conversion is slow during the continuous lithiation/delithiation of FeF_x cathodes, a solid-liquid F channel of the O-doped FeF_x strategy was proposed to activate the highly reversible reaction.[123] The solid-liquid F channel is constructed by a tris(pentafluorophenyl) borane (TPFPB) anionic receptor dissolved in ether electrolyte, which TPFPB molecule as F^- receptor by dissociating passivated LiF to form a solvated $[TPFPB\text{-}F]^-$ intermediate at the multiphase interface (Figure 8a). It cleverly avoids the difficult solid-solid conversion process and provides a convenient F^- transport channel between LiF and Fe. The construction of solid-liquid channel and fluorinated CEI layer derived from electrolyte promoted more convenient F^- transport and reversible lithiation/delithiation in the O-doped FeF_x cathodes. The assembled cell delivered a capacity of 472 mAh g^{-1} after 100 cycles at 0.1 A g^{-1} (Figure 8b).

ILs electrolytes have a more desirable safety than organic electrolytes due to their low vapor pressure and no gas generation.[124,125] For the FeF_x cathodes, there is no systematic study based on ILs electrolytes. In addition, the viscosity of ILs is higher than that of ordinary liquid organic electrolytes, which significantly impacts the charge transfer process during multi-electron conversion reactions.

To clarify the above issues, Tawa et al.[126] investigated the charging/discharging behavior of the FeF_3 cathode using ILs electrolytes (LiFSI in 1-ethyl-3-methylimidazolium) at 363 K. The results show that increasing the operating temperature is an effective way to overcome the large overpotential and slow reaction kinetics of FeF_x cathodes in ILs electrolytes. Recently, 1 M LiFSI in $Pyr_{1,3}FSI$ as an ILs electrolyte was introduced to FeF_2 cathode.[38] Compared with the liquid organic electrolyte, except for the largely irreversible capacity loss caused by CEI layer during the first discharge process. The ILs (LiFSI in

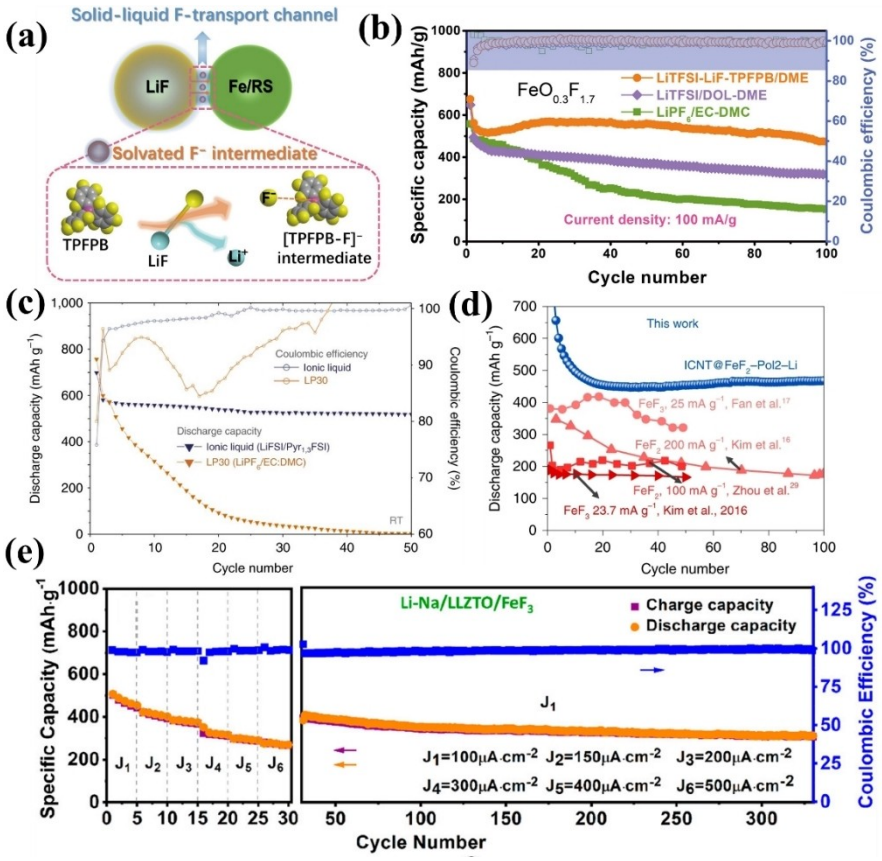

Figure 8. Strategy of electrolyte engineering designs: a) Illustration of formation of solid-liquid F-transport channel between LiF and Fe species. b) cycling performance of O-doped FeF_x with different electrolytes. Reproduced with permission from Ref. [123]. Copyright (2022) AAAs. c) Discharge capacity of FeF_2 electrode with the Ionic liquid electrolyte (LiFSI in $Pyr_{1,3}FSI$) and convention organic electrolyte (1 M $LiPF_6$ in EC/DMC). Reproduced with permission from Ref. [38]. Copyright (2020) Springer Nature. d) Discharge capacity of FeF_2 in LIFSI/PEO solid polymer electrolyte. Reproduced with permission from Ref. [130]. Copyright (2020) Springer Nature. e) Rate performance and cycling stability of the solid-state battery. Reproduced with permission from Ref. [131]. Copyright (2020) American Chemical Society.

$Pyr_{1,3}FSI$) electrolytes achieve excellent cycling stability of 570 mAh g^{-1} with over 90% capacity retention (Figure 8c). Transmission electron microscopy showed that the ILs (LiFSI in $Pyr_{1,3}FSI$) electrolyte forms a 10 nm-thick surface CEI layer, preventing Fe particles dissolution, demonstrating the great potential of ILs electrolytes to overcome the inherent issues of FeF_x cathodes.

Liquid electrolytes are widely used in LIBs due to their high ionic conductivity and good electrode wettability. The traditional organic electrolyte is flammable and easy to leak, which brings great safety risks to LIBs. In addition, the inability of liquid electrolytes to inhibit the dendrites formation also prevents the lithium metal anodes application.[127–129] Since it can improve safety and inhibit dendrite formation, researchers are increasingly turning to the study of solid-state electrolytes. It is expected to fundamentally solve the safety of current liquid-based LIBs.

Recently, a bis(trifluoromethane)sulfonimide lithium salt (LiTFSI)/poly(ethylene)oxide (PEO) was applied to FeF_x cathodes as a solid polymer electrolyte.[130] The formation of a mechanically stable electrolyte interface layer on the FeF_2 cathode is the key to enhancing the stability of the electrode structure. Therefore, the electrode delivered a reversible capacity of 450 mAh g^{-1} over 100 cycles at 50 °C (Figure 8d). Lately, a garnet-based solid-state electrolyte was successfully prepared and applied to FeF_x electrodes for the first time.[131] Coupled with Li–Na alloy with good interface wettability and stability, the FeF_3-based solid-state battery achieves a high reversible specific capacity of 500 mAh g^{-1} and cycle stability of 300 cycles operated at 60 °C (Figure 8e). To further enhance the reversibility of fluoride converted solid-state batteries, an alloyable viscous fluid method is used for lithium/garnet interfacial wetting.[132] Super-assembled phenide polymers with liquid metal properties can in-situ construct hybrid ion/electron conduction networks, resulting in a significant reduction of the interfacial resistance to 6 Ω cm^2. The confinement and compaction of the multi-phase reaction products by the garnet electrolyte enable a high-rate performance (330 mAh g^{-1} even at 2 C). Moreover, the remarkable electrochemical stability of the halide-based solid-state electrolyte allows for the complete conversion of FeF_2 cathode.[133] It is shown that the same concept employing halide-based solid-state electrolytes can be extended to other conversion cathodes to overcome the challenges inherent in metal fluorides.

5. Conclusion and Outlook

The multi-electron reaction mechanism results in the high energy density of FeF_x with promising development. However, in view of practical applications, compared with the current insertion type cathodes, the gravimetric/volumetric energy density of FeF_x cathodes is far from meeting the current requirements. Their outstanding performance largely depends on the synthesis of cathode materials. In this review, we outlined the advances of FeF_x materials as high-energy cathodes in LIBs. The working principle and remaining challenges are described, and synthetic fluorination routes utilizing different types of fluorine sources are summarized. Among them, ILs, HF solutions and other solid fluorine sources are limited by the difficulty of accurately constructing nanoscale uniform FeF_x during the fluorination process. In particular, four optimization methods for improved FeF_x performance, including conductive matrix, heteroatom doping, surface modification and electrolyte engineering, are discussed in detail. This review may broaden understanding of the design and optimization of high-energy density cathode materials.

Although the kinetic sluggishness of multiphase heterogeneous interface, difficult space limitation of active materials and serious parasitic side reactions of interfaces have been effectively controlled by various modification strategies. There are still serious challenges to achieving potential applications. The following aspects will be further addressed to achieve a high energy density of FeF_x cathodes:

1) For FeF_x cathode, an in-depth study of the detailed reaction evolution mechanism is still lacking. The real reaction process and materials degradation mechanism have not been uniformly understood since the conversion reaction is a multi-step reaction process. Combining theoretical calculations and in-situ scale observations enables an in-depth understanding of material properties and reaction mechanisms for the design and performance optimization of FeF_x cathodes.
2) The electrode/electrolyte interface is critical to the electrochemical behaviour. Unlike sulfur cathodes in lithium sulfur batteries, there is no direct solubility problem. However, the interfacial reactions of FeF_x cathode with the electrolyte are also crucial during cycling. The Fe nanodomain formed by the conversion reaction enlarges the contact area with the electrolyte, resulting in direct contact between the cathode and electrolyte. Owing to the lack of stable CEI layers, except for aggravating its own dissolution problems, the catalytic property easily leads to interfacial parasitic reactions related to the electrolyte. Consequently, a controllable interface layer can be optimized based on its electron/ion conductivity and protection effectiveness.
3) From the perspective of electrolyte solvents, carbonate solvents may not construct a beneficial interfacial layer to support the long-term conversion reactions. For ether-based solvents, although efficient bulk phase ion transport is conducive to improving conversion kinetics, its inferior oxidation stability will be a major hinder in matching FeF_x cathodes operated at high potentials. Therefore, the rational regulation of lithium salts, solvents, and additive components, ensuring the electrochemical stability of the electrolyte and the rapid bulk kinetics, as well as constructing a robust CEI layer on the cathode side, has been beneficial in achieving sustainable, efficient, and stable conversion reactions of FeF_x cathodes.

Acknowledgements

This research was supported by the National Natural Science Foundation of China (22279101, 22172117 and 52072298), the Natural Science Foundation of Shaanxi (2020JC-41 and 2021TD-15), Scientific Research Program Funded by Education Department of Shaanxi Provincial Government (22JP056).

Conflict of Interest

The authors declare no conflict of interest.

Data Availability Statement

The data that support the findings of this study are available from the corresponding author upon reasonable request.

Keywords: cathode materials · conversion-type cathode · iron fluoride · lithium-ion batteries · metal fluorides

[1] B. Dunn, H. Kamath, J. M. Tarascon, *Science* **2011**, *334*, 928–935.
[2] Z. Yang, J. Zhang, M. C. Kintner-Meyer, X. Lu, D. Choi, J. P. Lemmon, J. Liu, *Chem. Rev.* **2011**, *111*, 3577–3613.
[3] J. Xia, Z. Wang, N. D. Rodrig, B. Nan, J. Zhang, W. Zhang, B. L. Lucht, C. Yang, C. Wang, *Adv. Mater.* **2022**, *34*, 2205229.
[4] Q. Li, X. Yu, H. Li, *eTransportation* **2022**, *14*, 100201.
[5] Y.-S. Zhang, B.-M. Zhang, Y.-X. Hu, J. Li, C. Lu, M.-J. Liu, K. Wang, L.-B. Kong, C.-Z. Zhao, W.-J. Niu, *Energy Storage Mater.* **2021**, *34*, 45–52.
[6] J. W. Choi, D. Aurbach, *Nat. Rev. Mater.* **2016**, *1*, 1–16.
[7] J. L. Li, Z. J. Du, R. E. Ruther, S. J. An, L. A. David, K. Hays, M. Wood, N. D. Phillip, Y. P. Sheng, C. Y. Mao, S. Kalnaus, C. Daniel, D. L. Wood, *JOM* **2017**, *69*, 1484–1496.
[8] W. Li, R. Long, H. Chen, J. Geng, *Renewable Sustainable Energy Rev.* **2017**, *78*, 318–328.
[9] J.-H. Huang, X. L. Dong, Z. W. Guo, Y. Y. Ma, Y. R. Wang, Y. G. Wang, *J. Electrochem.* **2020**, *26*, 486.
[10] M. R. Palacín, A. de Guibert, *Science* **2016**, *351*, 1253292.
[11] B. Liu, R. Y. Fang, D. Xie, W. K. Zhang, H. Huang, Y. Xia, X. L. Wang, X. H. Xia, J. P. Tu, *Energy Environ. Mater.* **2018**, *1*, 196–208.
[12] Q. S. Wang, P. Ping, X. J. Zhao, G. Q. Chu, J. H. Sun, C. H. Chen, *J. Power Sources* **2012**, *208*, 210–224.
[13] M. Wentker, M. Greenwood, J. Leker, *Energies* **2019**, *12*, 504.
[14] X. X. Wang, Z. R. Zhou, Q. Shan, Z. M. Zhang, J. Huang, Y. W. Liu, L. S. Chen, *J. Electrochem.* **2020**, *26*, 596.
[15] W. Liu, X. Li, D. Xiong, Y. Hao, J. Li, H. Kou, B. Yan, D. Li, S. Lu, A. Koo, *Nano Energy* **2018**, *44*, 111–120.
[16] Y. Hao, W. Liu, Q. Zhang, X. Wang, H. Yang, L. Kou, Z. Tian, L. Shao, H. M. K. Sari, J. Wang, *Nano Energy* **2021**, *88*, 106240.
[17] H. Maleki Kheimeh Sari, X. Li, *Adv. Energy Mater.* **2019**, *9*, 1901597.
[18] F. Wu, J. Maier, Y. Yu, *Chem. Soc. Rev.* **2020**, *49*, 1569–1614.
[19] F. X. Wu, G. Yushin, *Energy Environ. Sci.* **2017**, *10*, 435–459.
[20] J. Li, Q. Q. Yang, Y. X. Hu, M. C. Liu, C. Lu, H. Zhang, L. B. Kong, W. W. Liu, W. J. Niu, K. Zhao, Y. C. Wang, F. L. Cheng, Z. M. M. Wang, Y. L. Chueh, *ACS Sustainable Chem. Eng.* **2019**, *7*, 18375–18383.

[21] F. Badway, F. Cosandey, N. Pereira, G. Amatucci, *J. Electrochem. Soc.* **2003**, *150*, A1318–A1327.
[22] H. Li, G. Richter, J. Maier, *Adv. Mater.* **2003**, *15*, 736–739.
[23] M. C. Liu, J. Li, Q. Q. Yang, Y. Xu, L. B. Kong, R. J. Bai, W. W. Liu, W. J. Niu, Y. L. Chueh, *ACS Appl. Nano Mater.* **2019**, *2*, 2634–2641.
[24] L. Liu, M. Zhou, L. Yi, H. Guo, J. Tan, H. Shu, X. Yang, Z. Yang, X. Wang, *J. Mater. Chem.* **2012**, *22*, 17539–17550.
[25] L. Chen, Y. Xu, G. Cao, H. M. K. Sari, R. Duan, J. Wang, C. Xie, W. Li, X. Li, *Adv. Funct. Mater.* **2022**, *32*, 2107838.
[26] J. R. He, A. Manthiram, *Energy Storage Mater.* **2019**, *20*, 55–70.
[27] D. W. Su, D. Zhou, C. Y. Wang, G. X. Wang, *Adv. Funct. Mater.* **2018**, *28*, 1800154.
[28] F. Badway, F. Cosandey, N. Pereira, G. Amatucci, *J. Electrochem. Soc.* **2003**, *150*, A1318.
[29] F. Wu, V. Srot, S. Chen, M. Zhang, P. A. van Aken, Y. Wang, J. Maier, Y. Yu, *ACS Nano* **2020**, *15*, 1509–1518.
[30] L. Zhang, L. Yu, O. L. Li, S.-Y. Choi, G. Saeed, K. H. Kim, *J. Mater. Chem. A* **2021**, *9*, 16370–16383.
[31] Y. Su, J. Chen, H. Li, H. Sun, T. Yang, Q. Liu, S. Ichikawa, X. Zhang, D. Zhu, J. Zhao, L. Geng, B. Guo, C. Du, Q. Dai, Z. Wang, X. Li, H. Ye, Y. Guo, Y. Li, J. Yao, J. Yan, Y. Luo, H. Qiu, Y. Tang, L. Zhang, Q. Huang, J. Huang, *Adv. Sci.* **2022**, *9*, e2201419.
[32] M. Liu, J. Liu, B. Chen, T. Wu, G. Wang, M. Chen, Z. Yang, Y. Bai, X. Wang, *Small* **2022**, *18*, e2105193.
[33] H. M. Wang, S. S. Chen, C. L. Fu, Y. Ding, G. R. Liu, Y. L. Cao, Z. X. Chen, *ACS Mater. Lett.* **2021**, *3*, 956–977.
[34] X. Wang, G. Tan, Y. Bai, F. Wu, C. Wu, *Electrochem. Energy Rev.* **2021**, *4*, 35–66.
[35] F. Wu, H. Y. Yang, Y. Bai, C. Wu, *J. Energy Chem.* **2020**, *51*, 416–417.
[36] K. Karki, L. Wu, Y. Ma, M. J. Armstrong, J. D. Holmes, S. H. Garofalini, Y. Zhu, E. A. Stach, F. Wang, *J. Am. Chem. Soc.* **2018**, *140*, 17915–17922.
[37] K. Shimoda, M. Shikano, M. Murakami, H. Sakaebe, *J. Power Sources* **2020**, *477*, 228772.
[38] A. W. Xiao, H. J. Lee, I. Capone, A. Robertson, T. U. Wi, J. Fawdon, S. Wheeler, H. W. Lee, N. Grobert, M. Pasta, *Nat. Mater.* **2020**, *19*, 644–654.
[39] X. Hua, A. S. Eggeman, E. Castillo-Martinez, R. Robert, H. S. Geddes, Z. H. Lu, C. J. Pickard, W. Meng, K. M. Wiaderek, N. Pereira, G. G. Amatucci, P. A. Midgley, K. W. Chapman, U. Steiner, A. L. Goodwin, C. P. Grey, *Nat. Mater.* **2021**, *20*, 841.
[40] F. Wang, R. Robert, N. A. Chernova, N. Pereira, F. Omenya, F. Badway, X. Hua, M. Ruotolo, R. Zhang, L. Wu, V. Volkov, D. Su, B. Key, M. S. Whittingham, C. P. Grey, G. G. Amatucci, Y. Zhu, J. Graetz, *J. Am. Chem. Soc.* **2011**, *133*, 18828–18836.
[41] Y. Y. Zheng, S. Tawa, J. Hwang, Y. Orikasa, K. Matsumoto, R. Hagiwara, *Chem. Mater.* **2021**, *33*, 868–880.
[42] S. Tawa, Y. Sato, Y. Orikasa, K. Matsumoto, R. Hagiwara, *J. Power Sources* **2019**, *412*, 180–188.
[43] M. Liu, L. Liu, M. Li, B. Chen, H. Lei, H. Hu, X. Wang, *J. Alloys Compd.* **2020**, *829*, 154215.
[44] K. Kumagae, K. Okazaki, K. Matsui, H. Horino, T. Hirai, J. Yamaki, Z. Ogumi, *J. Electrochem. Soc.* **2016**, *163*, A1633–A1636.
[45] L. Li, R. Jacobs, P. Gao, L. Gan, F. Wang, D. Morgan, S. Jin, *J. Am. Chem. Soc.* **2016**, *138*, 2838–2848.
[46] Q. Huang, T. P. Pollard, X. L. Ren, D. Kim, A. Magasinski, O. Borodin, G. Yushin, *Small* **2019**, *15*, 1804670.
[47] D. Aurbach, *J. Power Sources* **2000**, *89*, 206–218.
[48] M. Sina, R. Thorpe, S. Rangan, N. Pereira, R. A. Bartynski, G. G. Amatucci, F. Cosandey, *J. Phys. Chem. C* **2015**, *119*, 9762–9773.
[49] D. Gordon, Q. Huang, A. Magasinski, A. Ramanujapuram, N. Bensalah, G. Yushin, *Adv. Energy Mater.* **2018**, *8*, 1800213.
[50] X. Wang, W. Gu, J. T. Lee, N. Nitta, J. Benson, A. Magasinski, M. W. Schauer, G. Yushin, *Small* **2015**, *11*, 5164–5173.
[51] P. Hagenmuller, *Inorganic solid fluorides: chemistry and physics*, Elsevier, **2012**.
[52] H. Groult, F. Leroux, A. Tressaud, *Modern Synthesis Processes and Reactivity of Fluorinated Compounds: Progress in Fluorine Science*, Elsevier, **2016**.
[53] K. Seppelt (Ed.), *Curious World of Fluorinated Molecules*, Elsevier, **2021**.
[54] C. Li, C. Yin, L. Gu, R. E. Dinnebier, X. Mu, P. A. van Aken, J. Maier, *J. Am. Chem. Soc.* **2013**, *135*, 11425–11428.
[55] K. Turcheniuk, D. Bondarev, G. G. Amatucci, G. Yushin, *Mater. Today* **2021**, *42*, 57–72.
[56] M. Liu, Q. Wang, B. Chen, H. Lei, L. Liu, C. Wu, X. Wang, Z. Yang, *ACS Sustainable Chem. Eng.* **2020**, *8*, 15651–15660.
[57] Y. T. Teng, S. S. Pramana, J. F. Ding, T. Wu, R. Yazami, *Electrochim. Acta* **2013**, *107*, 301–312.
[58] W. T. Gu, O. Borodin, B. Zdyrko, H. T. Lin, H. Kim, N. Nitta, J. X. Huang, A. Magasinski, Z. Milicev, G. Berdichevsky, G. Yushin, *Adv. Funct. Mater.* **2016**, *26*, 1507–1516.
[59] F. Wu, V. Srot, S. Chen, M. Zhang, P. A. van Aken, Y. Wang, J. Maier, Y. Yu, *ACS Nano* **2021**, *15*, 1509–1518.
[60] Z. Bai, H. Lin, J. Johnson, S. C. R. Gui, K. Imakita, R. Montazami, M. Fujii, N. Hashemi, *J. Mater. Chem. C* **2014**, *2*, 1736–1741.
[61] C. Li, L. Gu, S. Tsukimoto, P. A. van Aken, J. Maier, *Adv. Mater.* **2010**, *22*, 3650–3654.
[62] Y. Lu, Z. Wen, J. Jin, K. Rui, X. Wu, *Phys. Chem. Chem. Phys.* **2014**, *16*, 8556–8562.
[63] D. P. Cao, C. L. Yin, J. C. Zhang, C. L. Li, *Chinese Sci. Bull.* **2017**, *62*, 897–907.
[64] C. L. Li, L. Gu, J. W. Tong, S. Tsukimoto, J. Maier, *Adv. Funct. Mater.* **2011**, *21*, 1391–1397.
[65] L. Lu, S. Li, J. Li, L. Lan, Y. Lu, S. Xu, S. Huang, C. Pan, F. Zhao, *Nanoscale Res. Lett.* **2019**, *14*, 1–11.
[66] W. Gu, A. Magasinski, B. Zdyrko, G. Yushin, *Adv. Energy Mater.* **2015**, *5*, 1401148.
[67] Q. Chu, Z. Xing, J. Tian, X. Ren, A. M. Asiri, A. O. Al-Youbi, K. A. Alamry, X. Sun, *J. Power Sources* **2013**, *236*, 188–191.
[68] D. Deng, *ChemNanoMat* **2017**, *3*, 146–159.
[69] J. Zhu, D. Deng, *Angew. Chem. Int. Ed.* **2015**, *54*, 3079–3083; *Angew. Chem.* **2015**, *127*, 3122–3126.
[70] D. Dambournet, K. W. Chapman, M. Duttine, O. Borkiewicz, P. J. Chupas, H. Groult, *ChemistryOpen* **2015**, *4*, 443–447.
[71] M. Duttine, D. Dambournet, N. Penin, D. Carlier, L. Bourgeois, A. Wattiaux, K. W. Chapman, P. J. Chupas, H. Groult, E. Durand, *Chem. Mater.* **2014**, *26*, 4190–4199.
[72] Y. Li, F. Yao, Y. Cao, H. Yang, Y. Feng, W. Feng, *Electrochim. Acta* **2017**, *253*, 545–553.
[73] R. Ma, M. Wang, P. Tao, Y. Wang, C. Cao, G. Shan, S. Yang, L. Xi, J. C. Chung, Z. Lu, *J. Mater. Chem. A* **2013**, *1*, 15060–15067.
[74] L. P. Li, J. H. Zhu, M. W. Xu, J. Jiang, C. M. Li, *ACS Appl. Mater. Interfaces* **2017**, *9*, 17992–18000.
[75] J. Chun, C. Jo, S. Sahgong, M. G. Kim, E. Lim, D. H. Kim, J. Hwang, E. Kang, K. A. Ryu, Y. S. Jung, Y. Kim, J. Lee, *ACS Appl. Mater. Interfaces* **2016**, *8*, 35180–35190.
[76] Q. Cheng, Y. Pan, Y. Chen, A. Zeb, X. Lin, Z. Yuan, J. Liu, *Inorg. Chem.* **2020**, *59*, 12700–12710.
[77] Z. Sun, W. Fu, M. Z. Liu, P. Lu, E. Zhao, A. Magasinski, M. Liu, S. Luo, J. McDaniel, G. Yushin, *J. Mater. Chem. A* **2020**, *8*, 4091–4098.
[78] Z. Sun, M. Boebinger, M. Liu, P. Lu, W. Fu, B. Wang, A. Magasinski, Y. Zhang, Y. Huang, A. Song, *J. Power Sources* **2021**, *507*, 230281.
[79] W. B. Fu, E. B. Zhao, Z. F. Sun, X. L. Ren, A. Magasinski, G. Yushin, *Adv. Funct. Mater.* **2018**, *28*, 1801711.
[80] Z. Sun, M. Boebinger, M. Liu, P. Lu, W. Fu, B. Wang, A. Magasinski, Y. Zhang, Y. Huang, A. Song, M. T. McDowell, G. Yushin, *J. Power Sources* **2021**, *507*, 230281.
[81] Y. Han, J. Hu, C. Yin, Y. Zhang, J. Xie, D. Yin, C. Li, *J. Mater. Chem. A* **2016**, *4*, 7382–7389.
[82] R. de Pape, *C. R. Acad. Sci.* **1965**, *260*, 4527.
[83] A. Tressaud, J. Portier, R. D. Pape, P. Hagenmuller, *J. Solid State Chem.* **1970**, *2*, 269–277.
[84] H. Groult, S. Neveu, S. Leclerc, A.-G. Porras-Gutierrez, C. Julien, A. Tressaud, E. Durand, N. Penin, C. Labrugère, *J. Fluorine Chem.* **2017**, *196*, 117–127.
[85] W. Li, H. Groult, O. J. Borkiewicz, D. Dambournet, *J. Fluorine Chem.* **2018**, *205*, 43–48.
[86] J. Oh, E. Lim, J. Chun, C. Jo, *J. Power Sources* **2022**, *521*, 230935.
[87] J. Zhai, Z. Lei, K. Sun, S. Zhu, *Electrochim. Acta* **2022**, *423*, 140595.
[88] J. Zhang, L. Zhang, Y. Zhao, J. Meng, B. Wen, K. M. Muttaqi, M. R. Islam, Q. Cai, S. Zhang, *Adv. Energy Mater.* **2022**, *12*, 2200959.
[89] X. Y. Zhou, H. X. Sun, H. C. Zhou, Z. L. Xu, J. Yang, *J. Alloys Compd.* **2017**, *723*, 317–326.
[90] L. Zhang, L. Yu, O. L. Li, S.-Y. Choi, M. Kim, G. Saeed, S. Bo, K. H. Kim, *J. Power Sources* **2022**, *547*, 232014.
[91] Y. Yang, L. Gao, L. M. Shen, N. Z. Bao, *J. Alloys Compd.* **2021**, *873*, 159799.
[92] F. Wu, V. Srot, S. Chen, S. Lorger, P. A. van Aken, J. Maier, Y. Yu, *Adv. Mater.* **2019**, *31*, e1905146.
[93] J. R. Zhai, Z. Y. Lei, D. Rooney, K. N. Sun, *Electrochim. Acta* **2019**, *313*, 497–504.

[94] D. F. He, Y. L. Zhang, D. Cao, M. F. Sun, J. W. Xia, Y. Yang, Y. J. Ding, H. Q. Chen, *J. Alloys Compd.* **2022**, *909*, 164702.
[95] D. Gueon, J. T. Hwang, S. B. Yang, E. Cho, K. Sohn, D. K. Yang, J. H. Moon, *ACS Nano* **2018**, *12*, 226–233.
[96] Z. F. Sun, B. C. Wang, M. G. Boebinger, A. Magasinski, S. Jhulki, Y. W. Zhang, W. B. Fu, M. T. McDowell, G. Yushin, *ACS Appl. Mater. Interfaces* **2022**, *14*, 33447–33456.
[97] Q. Zhang, Y. Zhang, Y. Yin, L. Fan, N. Zhang, *J. Power Sources* **2020**, *447*, 227303.
[98] S. Liu, J. Chen, Y. Su, C. Zheng, D. Zhu, X. Zhang, X. Zhou, R. Ouyang, Q. Huang, Y. He, L. Tang, S. Li, Y. Qiu, G. Wang, Y. Tang, L. Zhang, Q. Huang, J. Huang, *Small* **2022**, *18*, e2202006.
[99] M. Liu, B. Chen, T. Wu, H. Li, X. Liu, G. Wang, M. Chen, Z. Yang, Y. Bai, X. Wang, *Chem. Eng. J.* **2022**, *451*, 138774.
[100] S. Wei, X. Wang, R. Yu, R. Zhang, M. Liu, Z. Yang, H. Hu, *J. Alloys Compd.* **2017**, *702*, 372–380.
[101] Y. Lu, S. Huang, Z. Zhang, X. Huang, L. Lan, L. Lu, S. Li, J. Li, C. Pan, F. Zhao, *Ionics* **2019**, *25*, 5221–5228.
[102] J. Su, W. Nong, H. W. Song, Y. Li, C. X. Wang, *J. Alloys Compd.* **2021**, *870*, 159395.
[103] M. Liu, J. Liu, B. Chen, T. Wu, G. Wang, M. Chen, Z. Yang, Y. Bai, X. Wang, *Small* **2022**, *18*, 2105193.
[104] K. M. Wiaderek, O. J. Borkiewicz, E. Castillo-Martinez, R. Robert, N. Pereira, G. G. Amatucci, C. P. Grey, P. J. Chupas, K. W. Chapman, *J. Am. Chem. Soc.* **2013**, *135*, 4070–4078.
[105] J. Ding, X. Zhou, C. Luo, H. Xu, J. Yang, J. Tang, *J. Mater. Sci.* **2022**, *57*, 1261–1270.
[106] J. Ding, X. Zhou, Q. Wang, C. Luo, J. Yang, J. Tang, *ChemElectroChem* **2020**, *7*, 4931–4935.
[107] X. Fan, E. Hu, X. Ji, Y. Zhu, F. Han, S. Hwang, J. Liu, S. Bak, Z. Ma, T. Gao, S. C. Liou, J. Bai, X. Q. Yang, Y. Mo, K. Xu, D. Su, C. Wang, *Nat. Commun.* **2018**, *9*, 2324.
[108] S. Hwang, X. Ji, S. M. Bak, K. Sun, J. Bai, X. Fan, H. Gan, C. Wang, D. Su, *ACS Nano* **2020**, *14*, 10276–10283.
[109] M. Chen, L. Zhao, X. Li, X. Liu, J. Zai, R. Qi, X. Qian, *Sci. China Mater.* **2022**, *65*, 629–636.
[110] S. Kim, J. Y. Liu, K. Sun, J. J. Wang, S. J. Dillon, P. V. Braun, *Adv. Funct. Mater.* **2017**, *27*, 1702783.
[111] X. F. Li, J. Liu, M. N. Banis, A. Lushington, R. Y. Li, M. Cai, X. L. Sun, *Energy Environ. Sci.* **2014**, *7*, 768–778.
[112] X. Meng, X. Q. Yang, X. Sun, *Adv. Mater.* **2012**, *24*, 3589–3615.
[113] E. B. Zhao, O. Borodin, X. S. Gao, D. N. Lei, Y. R. Xiao, X. L. Ren, W. B. Fu, A. Magasinski, K. Turcheniuk, G. Yushin, *Adv. Energy Mater.* **2018**, *8*, 1800721.
[114] C. F. Lin, X. L. Fan, A. Pearse, S. C. Liou, K. Gregorczyk, M. Leskes, C. S. Wang, S. B. Lee, G. W. Rubloff, M. Noked, *Chem. Mater.* **2017**, *29*, 8780–8791.
[115] J. Yang, Z. L. Xu, H. C. Zhou, J. J. Tang, H. X. Sun, J. Ding, X. Y. Zhou, *J. Power Sources* **2017**, *363*, 244–250.
[116] X. Zhou, J. Ding, J. Tang, J. Yang, H. Wang, M. Jia, *J. Electroanal. Chem.* **2019**, *847*, 113227.
[117] R. Zhang, X. Y. Wang, S. Y. Wei, X. Wang, M. Liu, H. Hu, *J. Alloys Compd.* **2017**, *719*, 331–340.
[118] J. Li, L. C. Fu, Z. W. Xu, J. J. Zhu, W. L. Yang, D. Y. Li, L. P. Zhou, *Electrochim. Acta* **2018**, *281*, 88–98.
[119] X. Fan, C. Luo, J. Lamb, Y. Zhu, K. Xu, C. Wang, *Nano Lett.* **2015**, *15*, 7650–7656.
[120] B. R. Wygant, L. C. Merrill, K. L. Harrison, A. A. Talin, D. S. Ashby, T. N. Lambert, *Adv. Sci.* **2022**, *9*, 2105803.
[121] H. Senoh, K. Matsui, M. Shikano, T. Okumura, H. Kiuchi, K. Shimoda, K. Yamanaka, T. Ohta, T. Fukunaga, H. Sakaebe, E. Matsubara, *ACS Appl. Mater. Interfaces* **2019**, *11*, 30959–30967.
[122] Q. Huang, K. Turcheniuk, X. L. Ren, A. Magasinski, D. Gordon, N. Bensalah, G. Yushin, *Adv. Energy Mater.* **2019**, *9*, 1803323.
[123] K. Chen, M. Lei, Z. Yao, Y. Zheng, J. Hu, C. Lai, C. Li, *Sci. Adv.* **2021**, *7*, eabj1491.
[124] A. Lewandowski, A. Swiderska-Mocek, *J. Power Sources* **2009**, *194*, 601–609.
[125] Z. Sun, B. Wang, M. G. Boebinger, A. Magasinski, S. Jhulki, Y. Zhang, W. Fu, M. T. McDowell, G. Yushin, *ACS Appl. Mater. Interfaces* **2022**, *14*, 33447–33456.
[126] S. Tawa, K. Matsumoto, R. Hagiwara, *J. Electrochem. Soc.* **2019**, *166*, A2105–A2110.
[127] C. Wang, J. Liang, J. T. Kim, X. Sun, *Sci. Adv.* **2022**, *8*, eadc9516.
[128] P. S. Lu, D. X. Wu, L. Q. Chen, H. Li, F. Wu, *Electrochem. Energy Rev.* **2022**, *5*, 1–46.
[129] Y. P. Pang, J. Y. Pan, J. H. Yang, S. Y. Zheng, C. S. Wang, *Electrochem. Energy Rev.* **2021**, *4*, 169–193.
[130] Q. Huang, K. Turcheniuk, X. L. Ren, A. Magasinski, A. Y. Song, Y. R. Xiao, D. Kim, G. Yushin, *Nat. Mater.* **2019**, *18*, 1343.
[131] Y. Zhang, J. Meng, K. Chen, H. Wu, J. Hu, C. Li, *ACS Energy Lett.* **2020**, *5*, 1167–1176.
[132] Y. Liu, J. Meng, M. Lei, Y. Yu, C. Lai, C. Li, *Adv. Funct. Mater.* **2022**, *33*, 2208013.
[133] B. Shao, S. Tan, Y. Huang, L. Zhang, J. Shi, X. Q. Yang, E. Hu, F. Han, *Adv. Funct. Mater.* **2022**, *32*, 2206845.

Manuscript received: November 10, 2022
Revised manuscript received: January 13, 2023
Accepted manuscript online: January 23, 2023
Version of record online: February 9, 2023